Weierstraß-Institut
für Angewandte Analysis und Stochastik

im Forschungsverbund Berlin e.V.

Preprint ISSN 0946 – 8633

Uniaxial, extensional flows in liquid bridges

Eberhard Bänsch[1], Christian P. Berg[2] , Antje Ohlhoff[3]

submitted: August 14th 2002

[1] Weierstrass Institute for
Applied Analysis and Stochastics
Mohrenstraße 39, D - 10117 Berlin
and
Freie Universität Berlin, Germany
email: baensch@wias-berlin.de

[2] Center of Applied Space
Technology and Microgravity (ZARM)
University of Bremen
Am Fallturm, D–28359 Bremen
email: cberg@zarm.uni-bremen.de

[3] Center of Applied Space
Technology and Microgravity (ZARM)
University of Bremen
Am Fallturm, D–28359 Bremen
email: ohlhoff@zarm.uni-bremen.de

No. 761
Berlin 2002

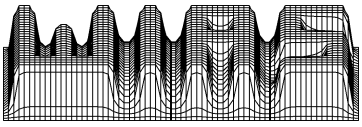

2000 *Mathematics Subject Classification.* 76D, 76E, 65M.

Key words and phrases. Uniaxial extensional flow, bridge stretching, microgravity, capillary forces, Navier-Stokes equations, free surface flow, finite elements, flow simulation..

Edited by
Weierstraß-Institut für Angewandte Analysis und Stochastik (WIAS)
Mohrenstraße 39
D — 10117 Berlin
Germany

Fax: + 49 30 2044975
E-Mail: preprint@wias-berlin.de
World Wide Web: http://www.wias-berlin.de/

Uniaxial, extensional flows in liquid bridges

By EBERHARD BÄNSCH [1], CHRISTIAN P. BERG [2] AND ANTJE OHLHOFF [2]

[1] Weierstrass Institute for Applied Analysis and Stochastics, Mohrenstrasse 39, D–10117 Berlin, and Freie Universität Berlin, Arnimallee 2–6, D–14195 Berlin, Germany
[2] Center of Applied Space Technology and Microgravity (ZARM), University of Bremen, Am Fallturm, Bremen, D–28359, Germany

(14 August 2002)

In this paper, we discuss the possibility to generate homogeneous flows with a nearly constant strain rate. This is achieved by stretching an almost cylindrical liquid bridge under microgravity. One key issue is the adaptation of the disk diameters in order to have always ideal boundary conditions. We first study the stretching of two different fluids both, by numerical and experimental means. The numerical results are compared with these experimental data resulting in a very good agreement. The numerical method is then used to study the behavior of liquid bridges for quite a large range of the flow parameters Capillary number Ca and Weber number We and detect those regimes with most suitable flow conditions.

Keywords: Uniaxial extensional flow, bridge stretching, microgravity, capillary forces, Navier-Stokes equations, free surface flow, finite elements, flow simulation.

1. Introduction

Linear flow fields are commonly used for rheological studies, e.g. to measure the fluid viscosity or the deformation behavior of the whole sample or components in it. The fluid properties may vary considerably depending on the specific linear flow type and the corresponding homogeneity of the flow field. In view of the experimental demands of rheological tests, the ideal uniaxial extensional flow field is characterized by a constant strain rate distribution both, in space and time.

The ideal uniaxial extensional flow field $\mathbf{v}$ with constant strain rate $\dot{\epsilon}_0$ in space and time would be of the form

$$\begin{aligned} v_r &= -\frac{1}{2}\dot{\epsilon}_0\, r, \\ v_\theta &= 0, \\ v_z &= \dot{\epsilon}_0 z, \end{aligned} \tag{1.1}$$

in a cylindrical coordinate system $(r,\, \theta,\, z)$. For an initially cylindrical fluid volume with length L_0 and radius R_0 this specific form of $\mathbf{v}$ implies

$$L(t) = L_0 \exp(\dot{\epsilon}_0 t), \tag{1.2}$$

$$R(t) = R_0 \exp(-0.5\, \dot{\epsilon}_0 t), \tag{1.3}$$

with $L(t)$ the length of the fluid volume and $R(t)$ its radius. In particular the liquid bridge is of cylindrical shape for all times.

However, the experimental realization of such a flow field causes severe difficulties in practice. Several attempts have been made towards this direction. For instance Chin

& Han 1979 and Mighri, Ajji & Carreau 1997 used a conical section of a transparent flow channel to investigate the deformation of emulsion droplets. Although this device is capable of providing an extensional flow within the entrance length of the conical channel, this extensional flow is predominantly non-constant and heterogeneous due to the developing velocity profile in the entrance region of the conical channel.

Because of the difficulties to generate homogeneous shear-free uniaxial extensional flows in convergent channels, mainly plane extensional flows were generated to perform droplet deformation experiments, see Stone 1994. A guidance to generate ideal plane extensional flow within a four-roll mill is given by Higdon 1993.

However, plane extensional flows are not optimal for the investigation of embedded axially symmetric emulsion droplets or particles due to the breaking of the 2d character of the flow, see also Berg 2002. For a comparison of e.g. droplet experiments with theoretical results uniaxial extensional flows are more adequate.

But even for stretched liquid bridges care must be taken to achieve a flow field with high quality, which depends on the actual inertia, capillary and viscous forces and appropriate boundary conditions. For instance Kröger *et al.* 1992 have shown that the contour deformation of an initially cylindrical liquid bridge between two unchanging endplates during stretching yields large variations of the local extension rates in space and time caused by *necking*.

To circumvent this effect and to obtain a constant extension rate at least in the middle of the bridge, Tirtaatmadja & Sridhar 1993 proposed to adjust the disk velocity profile. But even this attempt leads to a flow field which remains far from being homogeneous.

In this paper, we discuss the possibility to generate nearly homogeneous flows with an almost constant strain rate in a stretched fluid column by adapting the disk diameters in order to have always ideal boundary conditions to hold a cylindrical fluid bridge.

Even under μ–g conditions and with adjustment of the disk diameters the ideal extensional flow is not totally achievable due to the dynamic pressure gradient caused by the acceleration and capillary forces deforming the bridge contour, see Berg, Dreyer & Rath 1999. Instead, the real stretched fluid bridge is asymmetrically deformed in the direction of the accelerated support by forces owing to inertia and surface tension and will eventually pinch off.

The goal of our study is to investigate this behavior with respect to the flow parameters Capillary number Ca and Weber number We, see Section 2 below, and detect those regimes with most suitable flow conditions.

To this end we first study the stretching of two different fluids both, by numerical and experimental means. The numerical results are compared with these experimental data resulting in a very good agreement. The numerical method is then used to study the behavior of liquid bridges for quite a large range of the flow parameters Ca and We.

For the numerical simulation of the problem we use a finite element method with the following key ingredients: A variational formulation of the curvature of the free boundary, yielding an accurate, dimensionally independent and simply to implement approximation of the curvature; a stable time discretization, semi-implicit w.r.t. the treatment of the curvature terms, which on one hand avoids a CFL-like restriction of the time step as in common "explicit" treatments of the curvature terms and on the other hand decouples the computation of the geometry from that of the flow field. This approach has proven to be both efficient and robust with respect to the dimensionless parameters Ca, We, see Bänsch 2001 and also Section 3 below.

Let us mention some related work. Meissner 1969 developed the extensional rheometer, also known as rheotens test, which was modified by Maia *et al.* 1999. Matta & Tytus 1988 and Sridhar *et al.* 1991 pointed out the relevance of constant strain rate distributions in

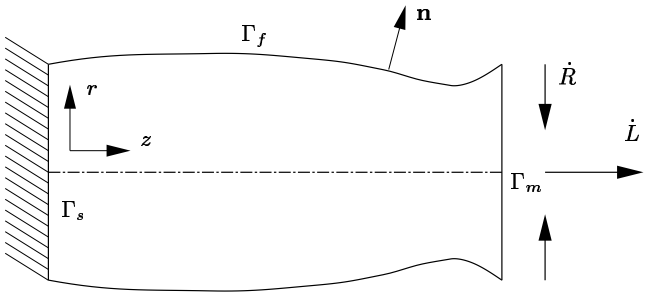

FIGURE 1. Setting and basic notation.

the full sample and developed the pioneering filament stretching device. Such stretching devices in turn were used by several research groups, e.g. Tirtaatmadja & Sridhar 1993, Berg, Kröger & Rath 1994, Spiegelberg, Ables & McKinley 1996 and Yao, Spiegelberg & McKinley 2000, to measure the extensional viscosity in macromolecular fluids.

In addition to the experimental work mentioned above, numerical simulations have been performed for instance in Gaudet, McKinley & Stone 1996, Spiegelberg, Ables & McKinley 1996 and Yao, Spiegelberg & McKinley 2000.

The rest of the article is organized as follows: in Section 2 we give the mathematical formulation of the problem. Section 3 briefly sketches the numerical method and Section 4 describes the experimental setup and experimental conditions. In Section 5 we first compare the experiments with corresponding simulations and then discuss a numerical parameter study for the dimensionless parameters Ca and We. Section 6 summarizes our results.

2. Problem formulation

2.1. *Mathematical formulation*

Denote by $\Omega = \Omega(t)$ the region occupied by the liquid. Ω is determined on one hand by the supporting devices Γ_s, Γ_m, which in turn are given by the setup of the stretching device and on the other hand by the a priori unknown free surface Γ_f (see figure 1). We consider an isothermal, incompressible and Newtonian fluid with constant density ρ and dynamical viscosity μ. Therefore the system can be described by the incompressible Navier-Stokes equations: Find a vector valued velocity field $\mathbf{v} = \mathbf{v}(t, \mathbf{x})$ and a pressure field $p = p(t, \mathbf{x})$ such that

$$\rho(\partial_t \mathbf{v} + \mathbf{v} \cdot \nabla \mathbf{v}) - \nabla \cdot \boldsymbol{\sigma} = \rho \mathbf{g} \quad \text{in } \Omega, \tag{2.1a}$$

$$\nabla \cdot \mathbf{v} = 0 \quad \text{in } \Omega. \tag{2.1b}$$

Here, $\mathbf{g} = g\,\mathbf{e}_z$ denotes the vector of gravity and $\boldsymbol{\sigma} = \boldsymbol{\sigma}(\mu\,\mathbf{v}, p)$ denotes the stress tensor

$$\boldsymbol{\sigma} = \mu\,\mathbf{D}(v) - p\mathbf{I} = \mu(\nabla \mathbf{v} + \nabla \mathbf{v}^T) - p\mathbf{I}.$$

Note that in order to avoid confusion, throughout the paper vector- as well as matrix-valued functions will be denoted by bold characters, whereas plain characters indicate scalars.

On the free surface Γ_f we have a balance of forces:

$$\boldsymbol{\sigma}\mathbf{n} = -\gamma \left(\frac{1}{R_1} + \frac{1}{R_2} \right) \mathbf{n} + \boldsymbol{\sigma}_{gas}\mathbf{n},$$

with γ the coefficient of surface tension, $1/R_1, 1/R_2$ the principle curvatures of Γ_f, $\mathbf{n}$ the (outward pointing) normal vector to Γ_f and $\boldsymbol{\sigma}_{gas}$ the stress tensor of the ambient gas phase. Since the dynamic part of the latter one is negligible we get

$$\boldsymbol{\sigma}\mathbf{n} = -\gamma\left(\frac{1}{R_1}+\frac{1}{R_2}\right)\mathbf{n} - p_{gas}\mathbf{n} \tag{2.2}$$

with the constant ambient pressure p_{gas}. Finally, the kinematic condition

$$\mathbf{v}\cdot\mathbf{n} = V_f,$$

with V_f the normal velocity of the free surface Γ_f, holds.

On the remaining parts Γ_s, Γ_m of the boundary, the fixed and moving support device, respectively, no-slip conditions for $\mathbf{v}$ hold.

2.2. *Non-dimensional, axially symmetric equations*

In view of the capillary driven flow in the bridge, the boundary dimension and the velocity, we set the problem into non-dimensional form by defining

$$\hat{\mathbf{x}} = \frac{1}{R_0}\mathbf{x}, \quad \hat{t} = \dot{\epsilon}_0 t, \quad \hat{\mathbf{v}} = \frac{1}{\dot{\epsilon}_0 R_0}\mathbf{v}, \quad \hat{p} = \frac{R_0}{\gamma}(p - p_{gas}).$$

Introducing the Weber number We, the Capillary number Ca, the Bond number Bo, and for convenience also the Reynolds number Re,

$$We = \frac{\rho R_0^3 \dot{\epsilon}_0^2}{\gamma}, \quad Ca = \frac{\mu R_0 \dot{\epsilon}_0}{\gamma}, \quad Bo = \frac{\rho\, R_0^2 g}{\gamma}, \quad Re = \frac{We}{Ca},$$

equation (2.1) becomes

$$We(\partial_{\hat{t}}\hat{\mathbf{v}} + \hat{\mathbf{v}}\cdot\hat{\nabla}\hat{\mathbf{v}}) - Ca\hat{\Delta}\hat{\mathbf{v}} + \hat{\nabla}\hat{p} = -Bo\,\mathbf{e}_z \quad \text{in } \hat{\Omega}, \tag{2.3a}$$

$$\hat{\nabla}\cdot\hat{\mathbf{v}} = 0 \quad \text{in } \hat{\Omega}, \tag{2.3b}$$

On the free surface $\hat{\Gamma}_f$ we have

$$-\hat{\boldsymbol{\sigma}}(Ca\,\hat{\mathbf{v}}, \hat{p})\mathbf{n} = \hat{\kappa}\,\mathbf{n}, \tag{2.3c}$$

$$\hat{\mathbf{v}}\cdot\mathbf{n} = \hat{V}_f, \tag{2.3d}$$

where $\hat{\kappa}$ is the sum of the principle curvatures of $\hat{\Gamma}_f$. In our case $Bo = 0$ (cp. Section 4.2), thus the non-dimensional system is characterized by the ratio of inertia and capillary forces We, the ratio of viscous and capillary forces Ca and the geometrical parameter $\Lambda_0 = \dfrac{L_0}{R_0}$. Since in what follows we are only working in non-dimensional quantities, from now on let us drop the " $\hat{}$ " for the sake of brevity and relabel the scaled variables again by $\mathbf{v}, p$ etc. unless otherwise stated. This abuse of notation will not lead to confusion.

Note that the fixed and moving boundaries are given in non-dimensional coordinates by

$$\Gamma_s = \{\mathbf{x} \mid 0 \le r \le \exp(-t/2), z = 0\}, \tag{2.4}$$

$$\Gamma_m = \{\mathbf{x} \mid 0 \le r \le \exp(-t/2), z = \Lambda_0 \exp(t)\}. \tag{2.5}$$

Since all data are axially symmetric and the flow is laminar we may assume an axially symmetric 2-dimensional situation, i.e.

$$\mathbf{v}(t,\mathbf{x}) = v_r(t,r,z)\mathbf{e}_r + v_z(t,r,z)\mathbf{e}_z, \quad p(t,\mathbf{x}) = p(t,r,z).$$

In cylindrical coordinates the non-dimensional problem now reads:

$$We(\partial_t v_r + \mathbf{v}\cdot\nabla v_r) + Ca\Big(-\Delta_{r,z} v_r + \frac{v_r}{r^2}\Big) + \partial_r p = 0, \tag{2.6a}$$

$$We(\partial_t v_z + \mathbf{v}\cdot\nabla v_z) - Ca\Delta_{r,z} v_z + \partial_z p = 0, \tag{2.6b}$$

$$\frac{1}{r}\partial_r(r\, v_r) + \partial_z v_z = 0, \tag{2.6c}$$

where $\Delta_{r,z}\, v = \frac{1}{r}\partial_r(r\partial_r v) + \partial_z^2 v$ is the Laplacian in cylindrical coordinates. On the free surface Γ_f we have

$$-Ca\begin{bmatrix} 2\partial_r v_r & \partial_r v_z + \partial_z v_r \\ \partial_r v_z + \partial_z v_r & 2\partial_z v_z \end{bmatrix}\begin{bmatrix} n_r \\ n_z \end{bmatrix} + p\,\mathbf{n} = \kappa\,\mathbf{n}. \tag{2.6d}$$

The kinematic condition reads

$$v_r n_r + v_z n_z = V_f. \tag{2.6e}$$

The non-slip conditions can be expressed as

$$v_z = \Lambda_0 \exp(t), \quad v_r = -\frac{1}{2} r \quad \text{on } \Gamma_m, \tag{2.6f}$$

$$v_z = 0, \qquad\quad v_r = -\frac{1}{2} r \quad \text{on } \Gamma_s. \tag{2.6g}$$

To close the system, initial conditions for $\mathbf{v}$ and for the initial fluid bridge $\Omega(0)$ are prescribed, see Section 4.2.

REMARK 1. *The situation described above refers to an ideal geometry, where for instance the radii of the two support devices and their time evolutions are equal. In practice, however, due to experimental inconveniences the radii and their behavior in time may differ slightly. Therefore, in order to get as close to the experimental settings as possible, in comparing the numerical simulations with the experiments we prescribe functions $R_s(t)$, $R_m(t)$ with data taken from the experiments, see also Section 4.2.*

3. Numerical method

Discretizing equations (2.6), the free boundary conditions (2.6*d*)–(2.6*e*) cause several problems, in particular the treatment of the curvature terms and in finding a stable and efficient time discretization.

To resolve these problems we use a variational formulation, where the free boundary condition (2.6*d*) is transformed to a boundary integral part of the bilinear forms. In the following we only sketch the basic ideas, for further reference see Bänsch 2001.

To proceed we write the momentum part of the Stokes equations (analogously for the Navier-Stokes equations) in the strong form, multiply by a solenoidal test function $\boldsymbol{\varphi}$ vanishing on the no-slip parts Γ_s, Γ_m of the boundary and integrate by parts. We get

$$\int_\Omega \Big\{ -Ca\,\Delta\mathbf{v} + \nabla p \Big\}\cdot\boldsymbol{\varphi} = \frac{Ca}{2}\int_\Omega D(\mathbf{v}) : D(\boldsymbol{\varphi}) - \int_\Omega p\nabla\cdot\boldsymbol{\varphi} - \int_{\Gamma_f} \mathbf{n}\cdot\boldsymbol{\sigma}\boldsymbol{\varphi},$$

where

$$D(\mathbf{v}) : D(\boldsymbol{\varphi}) := \sum_{i,j} D(\mathbf{v})_{i,j} D(\boldsymbol{\varphi})_{i,j}.$$

Taking into account the boundary condition (2.6d) gives

$$-\int_{\Gamma_f} \mathbf{n}\cdot\boldsymbol{\sigma}\boldsymbol{\varphi} = \int_{\Gamma_f} \kappa\,\mathbf{n}\cdot\boldsymbol{\varphi}.$$

A basic identity from differential geometry now yields

$$\int_{\Gamma_f} \kappa\,\mathbf{n}\cdot\boldsymbol{\varphi} = \int_{\Gamma_f} \underline{\nabla}\mathbf{x}\cdot\underline{\nabla}\boldsymbol{\varphi}, \tag{3.1}$$

where $\underline{\nabla}$ is the tangential gradient on Γ_f and $\mathbf{x}$ the position vector.

Summarizing we get

$$\int_{\Omega}\Big\{-Ca\,\Delta\mathbf{v}+\nabla p\Big\}\cdot\boldsymbol{\varphi} = \frac{Ca}{2}\int_{\Omega} D(\mathbf{v}):D(\boldsymbol{\varphi}) - \int_{\Omega} p\nabla\cdot\boldsymbol{\varphi} + \int_{\Gamma_f}\underline{\nabla}\mathbf{x}\cdot\underline{\nabla}\boldsymbol{\varphi}. \tag{3.2}$$

Note that since the situation is axially symmetric the above boundary integral can be expressed in parametric form as follows. Let Γ_f be given in parametric form by $\Gamma_f := \{r(s)\mathbf{e}_r + z(s)\mathbf{e}_z \mid s\in S\}$ with some parameter domain $S\subseteq I\!R$. Then for vector fields $\mathbf{f},\mathbf{h}$

$$\int_{\Gamma_f}\underline{\nabla}\mathbf{f}\cdot\underline{\nabla}\mathbf{h} = \int_S\Big\{\frac{Q(s)}{r(s)}f_r h_r \;+\; \frac{r(s)}{Q(s)}\big(\partial_s f_r\partial_s h_r + \partial_s f_z\partial_s h_z\big)\Big\}ds$$

with $Q(s) := \sqrt{\partial_s r(s)^2+\partial_s z(s)^2}$.

Although in our case a graph representation of the free surface Γ_f would be convenient, the above parametric form allows for a treatment of much more general Γ_f.

Time discretization

To discretize in time a semi-implicit coupling of the unknowns for the geometry Ω and the flow variables $\mathbf{v},p$ is used. More precisely, giving the values $\Omega^{k-1},\mathbf{v}^{k-1},p^{k-1}$ at the discrete time instant t_{k-1} we compute

Step 1: $\mathbf{v}^k$, p^k by solving (2.6a)–(2.6c) with boundary conditions (2.6d), (2.6f)–(2.6g) in Ω^{k-1}

Step 2: Γ_f^k by a discretized form of (2.6e): $\Gamma_f^k := \Gamma_f^{k-1} + (t_k - t_{k-1})\,\mathbf{v}^k$

Step 3: Γ_m^k by (2.5) and also the update of the domain by an *extension* of Γ^k into the interior, resulting in Ω^k

In **Step 1** the boundary condition (2.6d) is incorporated via the variational formulation according to (3.2). The curvature terms are treated in a semi-implicit way using the identity $\mathbf{x}^k = \mathbf{x}^{k-1} + (t_k - t_{k-1})\mathbf{v}^k$ of **Step 2** with $\mathbf{x}^{k-1},\mathbf{x}^k$ the position vectors of $\Gamma_f^{k-1},\Gamma_f^k$, respectively:

$$\int_{\Gamma_f^{k-1}}\underline{\nabla}\mathbf{x}^k\cdot\underline{\nabla}\boldsymbol{\varphi} = \int_{\Gamma_f^{k-1}}\underline{\nabla}\mathbf{x}^{k-1}\cdot\underline{\nabla}\boldsymbol{\varphi} + (t_k-t_{k-1})\int_{\Gamma_f^{k-1}}\underline{\nabla}\mathbf{v}^k\cdot\underline{\nabla}\boldsymbol{\varphi},$$

thus decoupling the flow computation from the determination of the geometry. The above algorithm leads to an unconditionally stable and efficient treatment of the free boundary conditions, see Bänsch 2001.

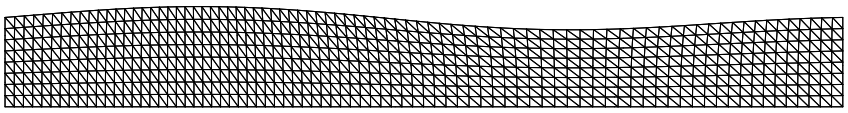

FIGURE 2. Typical (fine) triangular mesh used in the simulation.

For the extension of Γ^k into the interior in **Step 3** a smoothing of the triangulation by a discrete Poisson equation is used.

The computation of $\mathbf{v}^k, p^k$ is based on the axially symmetric version Tenhaeff 1997 of the method and implementation described in Bänsch 1991, Bänsch 1998. This code uses the fractional step θ–scheme in a variant as an operator splitting, which decouples two major numerical difficulties, the solenoidal condition and the nonlinearity, see Bristeau, Glowinski & Periaux 1986. The axially symmetric code solves for the unknowns (v_s, v_z) and p, where $v_s := \frac{v_r}{r}$. This scaling resolves the singularities of the operators at $r = 0$, and may be interpreted as a proper variational formulation of the axially symmetric Navier-Stokes equation in appropriately r–weighted Sobolev spaces, see also Lailly 1976.

Spatial discretization

To discretize in space the Taylor-Hood element, i.e. piecewise quadratic, globally continuous elements for $\mathbf{v}$ and piecewise linear, globally continuous elements for p, are used on triangular grids.

Some care must be taken to deal with the rather large aspect ratios encountered during stretching. To this end we use meshes that are *condensed* in the z–direction initially. Moreover, while moving the mesh from one time-step to another, a smoothing operator maintains mesh regularity, see above.

Code validation

The code was validated with examples for Newtonian fluids from Zhang, Padgett & Basaran 1996 and Yao & McKinley 1998. Furthermore, the examples in Section 5 were computed using several different meshes and time step sizes to make sure that the discretization error was sufficiently small.

It may be noteworthy that due to the higher spatial approximation order of the Taylor-Hood element and the accurate approximation of the curvature terms only rather coarse meshes were needed.

Figure 2 shows a typical mesh used in the simulations.

4. Experimental approach

4.1. *Setup and procedure*

An experimental setup was used to generate extensional flow fields by stretching a large cylindrical liquid bridge. The bridge had sufficiently large dimensions to measure its extensional viscosity by the forces at the endplates, as done by Berg, Kröger & Rath 1994, or to carry macroscopic particles such as fibers or emulsion droplets for orientation and deformation experiments, performed by Berg 2002. The goal of the setup was to generate a maximum homogeneous flow field and constant extension rates in space and time during stretching. For this reason, some technical effort was necessary to provide optimal flow conditions.

The stretching of the liquid bridge was performed under microgravity at the drop tower of Bremen. The microgravity environment during stretching was necessary to eliminate

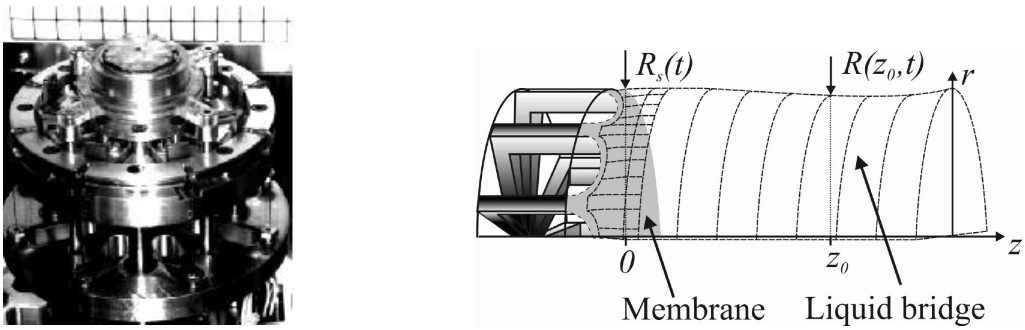

FIGURE 3. Supporting device to adapt the membrane radius to the actual bridge length; apparatus (left) and sketch of the device (right).

body forces owing to hydrostatic pressure. The liquid bridge was held exclusively between two almost circular concentric support membranes, which stretched the liquid by temporally controlled acceleration.

The core of the apparatus were two membrane reduction devices consisting of eight segments each, see figure 3, to adapt the membrane radius $R(t)$ to the actual length $L(t)$ of the liquid bridge according to (1.2), (1.3). One device was fitted to a linear slider on the right hand side whereas the left one had a fixed position. The initial size of the liquid bridge was $30\,mm$ in length and $15\,mm$ in radius. Adaptation of the radius was possible to a minimum of $5\,mm$ and a fluid length of $270\,mm$. The stretching rate was $\dot{\epsilon}_0 = 0.6/s$ in our experiments.

A typical experimental run, using castor oil (see table 1) in this example, is presented in figure 4. Picture (a) shows the liquid bridge before the onset of stretching, where the bridge is held between the membranes under microgravity conditions. The bridge is almost cylindrical before stretching and two immiscible emulsion droplets were placed inside the bridge to investigate their deformations in extensional flow in this particular experimental run.

In the following pictures (b)–(d), the supporting device on the right hand side stretches the bridge for $3.5s$ with exponentially increasing velocity according to (1.2). Simultaneously, the support membranes decrease their radii exponentially to adapt the fluid boundaries to the actual bridge length.

During stretching, an asymmetrical deformation in the direction to the accelerated support device can be seen, which, as we will show in Section 5, is typical and caused by forces owing mainly to inertia in this parameter range ($Ca = 0.179$, $We = 0.0325$).

4.2. *Experimental conditions*

In the microgravity environment residual accelerations caused by experimental disturbances occurred in the range between $10^{-6}\,g$ to $10^{-2}\,g$. According to the microgravity experiments in Berg 2002, disturbances greater than $10^{-6}\,g$ were irregular and damped out within less than $10^{-5}s$. These short disturbances initiated waves from the membranes into the liquid bridge. However, caused by viscous dissipation, the waves spatially faded away within less than $0.1\,mm$ and did not disturb the full bridge. Thus, only residual accelerations at about $10^{-6}\,g$ loaded the bridge with small hydrostatic pressure differences, characterized by Bond numbers less than $Bo = 10^{-4}$. These small hydrostatic pressure differences were irrelevant in all experiments compared to capillary, viscous or inertia effects and were therefore neglected in the simulations.

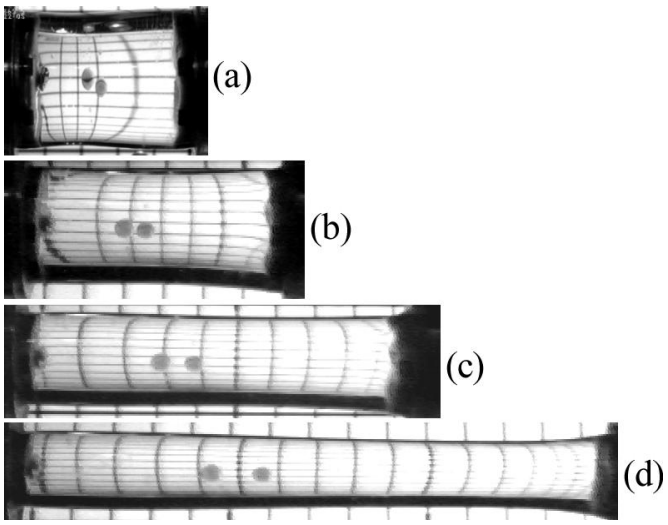

FIGURE 4. Initial and stretched bridge of castor oil Fluid 1 at $t = 0.0$ (a), $t = 0.444$ (b), $t = 0.888$ (c), $t = 1.344$ (d), respectively; time in dimensionless units.

	μ $[Pa \cdot s]$	γ $[10^{-3} N/m]$	ρ $[kg/m^3]$	$\dot{\epsilon}_0$ $[1/s]$	Λ_0 $[-]$	τ $[-]$	Ca $[-]$	We $[-]$
Fluid 1	0.71	35.7	954	0.6	2	0.115	0.179	0.0325
Fluid 2	9.7	21.3	975	0.6	2	0.151	4.099	0.0556

TABLE 1. Characteristics of the fluids (at $25°C$): μ the dynamical viscosity, γ the coefficient of surface tension, ρ the density; geometrical quantities: $\dot{\epsilon}_0$ the stretching rate, Λ_0 the initial aspect ratio, τ the (dimensionless) relaxation time , see (4.1); dimensionless parameters: Ca, We the Capillary and Weber numbers, respectively.

Two different liquids with medium and high viscosity, respectively, were used in the experiments. The following fluids were used:

- Fluid 1: castor oil, Lechner & Crebert GmbH, Mannheim, Germany,
- Fluid 2: a highly viscous silicon fluid, Dow Corning 200, Dow Chemical Comp., USA,

see also tabular 1 for the properties of both fluids.

Both fluids allowed to perform experiments maintaining almost cylindrical contours with small deformations during stretching, cp. figure 4. The resulting differences in deformations between the two fluids were mainly caused by the different Capillary numbers for Fluid 1 and Fluid 2.

For a precise comparison between experiment and numerical simulation, the real, opposed to completely ideal, experimental boundary conditions were taken into account. Since the liquid bridges were hold exclusively by the membranes, the shape of the membranes determined the liquid boundaries Γ_s, Γ_m. The areas of the membranes and a small part at the sides of the membranes were wetted by the liquid without a sharp edge. Moreover, remnants of sealing compound, which was used to insulate the device (which had to be closed under $1g$ conditions before the experimental run), were attached to the moving membrane resulting in an increased effective radius. Therefore, the actual liquid

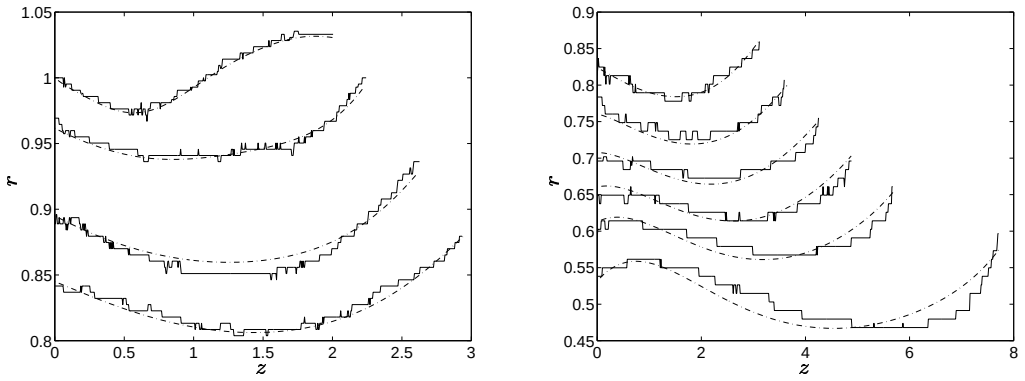

FIGURE 5. Fluid 1: Bridge shape at time instants $t = 0.000$, $t = 0.144$, $t = 0.288$, $t = 0.396$ (left) and $t = 0.444$, $t = 0.600$, $t = 0.744$, $t = 0.888$, $t = 1.04$, $t = 1.34$ (right), from top to bottom,respectively; time in non-dimensional units; experiment (solid) and simulation (dash–dotted).

radii $R_s(t)$ of Γ_s and $R_m(t)$ of Γ_m at the membrane positions during stretching were measured and imposed as boundary conditions in the numerical simulations instead of (2.5).

Moreover, the experimental procedure to provide the initial liquid bridges lead to concave-convex shaped contours, cp. figures 5 and 6. Also small losses of liquid for the initial bridges could not be totally avoided. This is why the initial liquid bridges contained always about only 96% fluid volume of the ideal cylindrical bridge. The numerical simulations were thus started with the corresponding initial shapes, which were measured and then interpolated by a polynomial fit of the order 7 and 8 for Fluid 1 and Fluid 2, respectively.

Furthermore, in order to avoid infinite forces at initial we defined a start-up phase by imposing $\mathbf{v}(0,\cdot) = 0$ and defining the time dependent boundary condition

$$v_z(t,\cdot) = \Lambda_0 \frac{d}{dt} \exp(t(1 - \exp(-t/\tau))) \quad \text{on } \Gamma_m, \tag{4.1}$$

which asymptotically approaches the "ideal" function $v_z = \Lambda_0 \exp(t)$ on the time scale τ. The (dimensionless) relaxation time τ was fitted to measurements from the experiments, see Berg 2002. The fitted values for τ for Fluid 1 and Fluid 2 are listed in tabular 1.

5. Results

5.1. *Comparison of experimental and numerical results*

As a first step in our investigation we compared the experimental results for Fluid 1 and Fluid 2 with corresponding simulations. The experiments with Fluid 1 and Fluid 2 were performed for $0 \leq t \leq 1.344$ and $0 \leq t \leq 2.1$, respectively, in non-dimensional units.

During the time evolution, the stretched bridges were recorded by a video camera with wide angle lens, which allowed total views of the bridge to a maximum length of $115\,mm$ (Fluid 1) and $245\,mm$ (Fluid 2), see figures 8 and 9. Moreover, a second camera provided a closer view of the accelerated bridges up to time $t = 0.444$. The contours of the bridge surface were evaluated reliably by digital image processing, which identified the bridge shape by a strong gradient in the pixel brightness. Because of the different

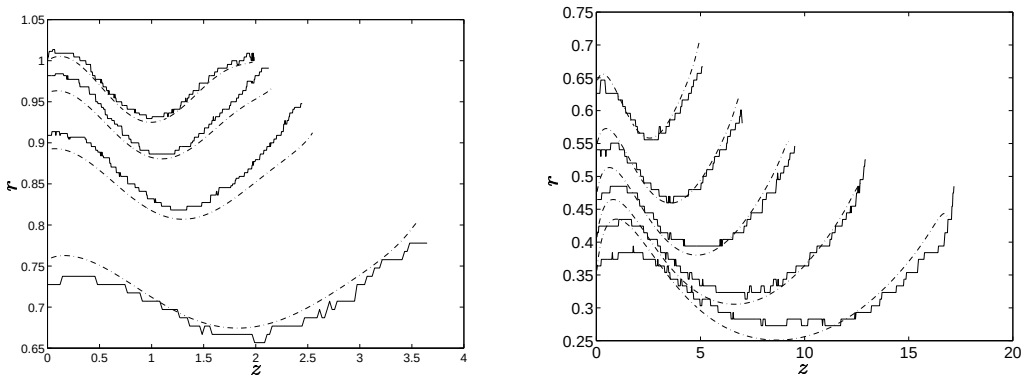

FIGURE 6. Fluid 2: Bridge shape at time instants $t = 0.000$, $t = 0.144$, $t = 0.288$, $t = 0.576$ (left) and $t = 0.888$, $t = 1.200$, $t = 1.488$, $t = 1.800$, $t = 2.064$ (right), from top to bottom,respectively; time in non-dimensional units; experiment (solid) and simulation (dash–dotted).

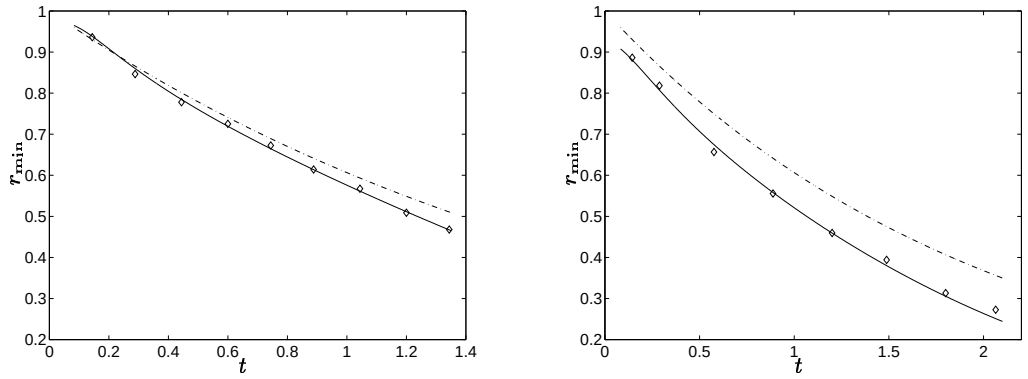

FIGURE 7. Minimum radius of the bridge versus time; experiment (diamonds), simulation (solid) and $\exp(-0.5\,t)$ (dashed–dotted); Fluid 1 (left) and Fluid 2 (right).

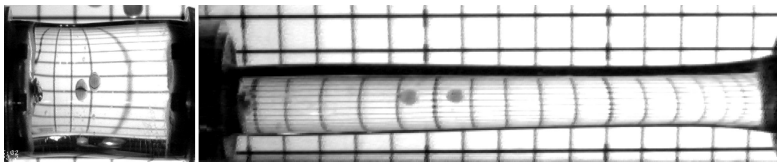

FIGURE 8. Initial and stretched bridge of castor oil (Fluid 1) at $t = 0.0$ (left) and $t = 1.344$ (right), respectively; time in dimensionless units.

image resolutions of the two cameras (small and wide angle lenses), stronger pixel steps occur in the contour images for $t > 0.444$, cp. figure 5 and figure 6.

The transient bridge deformation during stretching can be subdivided into two parts. In the first time period the capillary pressure tries to stabilize the bridge contour to a cylindrical shape of constant mean curvature. A first rough estimate of this time interval is determined by the stability limit of a stationary liquid bridge, i.e. the aspect ratio $\Lambda(t) = L(t)/R(t) \leq 2\pi$, which was already studied by Plateau 1863 and Rayleigh 1878.

During this period, the initial deformation re-orientates and relaxes, delayed by viscous forces. In the case of Fluid 1, the deformation changes from a concave-convex shape to

FIGURE 9. Initial and stretched bridge of silicon fluid (Fluid 2) at $t = 0.0$ (left) and $t = 1.344$ (right), respectively; time in dimensionless units.

a purely concave shape. Moreover, capillary forces stabilize the bridge contour, counteracting the dynamic pressure difference caused by the acceleration of the flow.

Beyond the stability limit, in the remaining stretching period, the capillary and the dynamic pressures deform the bridge contour. A significantly convex-concave shape in direction to the accelerated membrane on the right hand side arises. This typical bridge contour appears during stretching because of the negative pressure gradient in direction to the accelerated membrane. This typical convex-concave shape is clearly visible in figure 5. Eventually, the instability leads to a breakup of the bridge.

These two deformation processes, firstly reorientation by capillary pressure and then deformation by capillary and dynamic pressure differences, are clearly visible for Fluid 1. Both processes also appear for Fluid 2. However, due to the higher viscosity of this liquid, the reorientation and convex-concave deformation are more delayed and the transition between the two phases is less pronounced.

The numerical simulations are capable to reliably describe the transient deformation during the bridge stretching of Fluid 1 and 2. Figures 5 and 6 show that, in view of the real initial fluid volume and the measured membrane radii $R_s(t)$ and $R_m(t)$, the numerical results are in quite a good agreement to the experimental contours. More precisely, the experimental uncertainty of the recording device is 2 pixels and the agreement of the numerical results is of the same order of magnitude over most parts of the bridge and at almost all times.

From the good numerical reproduction of the transient bridge deformations in figures 5.1 and 5.2 we deduce that also the capillary, inertia and viscous forces during reorientation and deformation are accurately captured.

Since the bridge stretches with exponentially increasing velocity and the deformations are also growing in time, differences between simulated and experimental data are expected to be amplified in time. The small differences between numerical and experimental data at nearly all times is again an indication of the quality of the numerical method.

A commonly used parameter to characterize the bridge deformation is the minimum radius of the deformed bridge versus time, shown for our examples in figure 7. There, the actual radii, experimental as well as numerical, are compared to the ideal case of $R(t) = \exp(-0.5\,t)$. The deviation from this exponential is an expression for the bridge deformation. Figure 7 again confirms the reliability of the numerical results, expressed by the good agreement of the minimum radius to the experimental data.

In the next section, we discuss a parameter variation, to identify the forces acting in a stretched fluid bridge and the corresponding bridge shapes.

5.2. *Parameter variations and bridge shapes*

We investigated bridge stretching and the corresponding flow quality for a field of various Capillary and Weber numbers, shown in figure 10 together with a nomenclature '1' – '30'. The parameters were chosen to characterize the bridge stretching at realistic fluid properties and bridge dimensions.

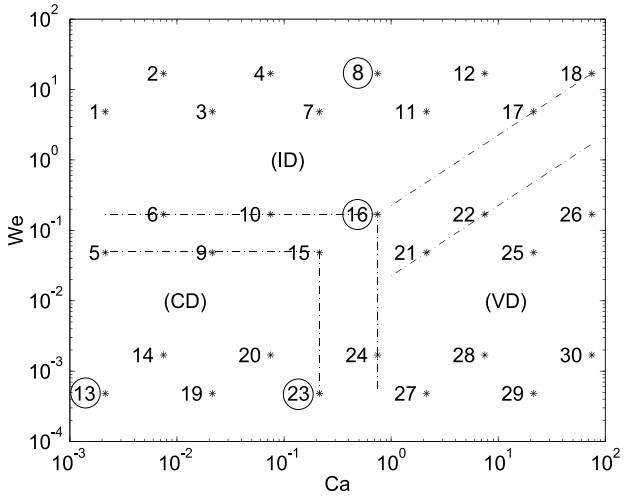

FIGURE 10. Parameter field, numbering of the numerical experiments; the dash-dotted lines mark the respective transition regions between capillary dominated (CD), viscosity dominated (VD) and inertia dominated (ID) flows. Marked examples 8, 13, 16, and 23 are discussed in detail below.

no.	liquid	μ $[Pa \cdot s]$	γ $[10^{-3} N/m]$	ρ $[kg/m^3]$	$\dot{\epsilon}_0$ $[1/s]$
1	water	0.0001	72	998	10
13	85 % glycerol–water	0.1129	66	1123	0.1
18	silicon fluid	10	21	975	10
30	silicon fluid	1025	21	976	0.1

TABLE 2. Some physical fluids in the parameter field.

The initial aspect ratio Λ_0 was chosen $\Lambda_0 = 2$ and the relaxation time τ from (4.1) was set to $\tau = 0.012$ for all examples. The initial bridge shape was chosen to be of ideal cylindrical form.

Physically, the parameter field can be interpreted for example in the following way: fixing the initial bridge radius to $R_0 = 15\,mm$, the stretching rates are varied between $0.1/s$ and $10/s$. The surface tension and viscosity are varied in the range of $20 \cdots 70\,mN/m$ and $0.001 \cdots 1000\,Pa{\cdot}s$, respectively, while keeping the density constant at about $1000\,kg/m^3$. Compare also table 2, where some possible physical fluids are identified within the parameter field.

Anticipating the result of our study, the parameter field can be subdivided into three major regimes:

- *capillary dominated flow*, characterized by $Ca \ll 1, We \ll 1$,
- *viscosity dominated flow*, $Ca > \mathcal{O}(0.1)$, $Re < \mathcal{O}(0.1)$,
- *inertia dominated flow*, $We > \mathcal{O}(0.1)$, $Re > \mathcal{O}(0.1)$.

The field could be considerably extended to other bridge dimensions and strain rates, but systematic changes of the flow quality and the deformation behavior are expected only at the transition between the capillary, viscosity or inertia dominated flow regimes, respectively.

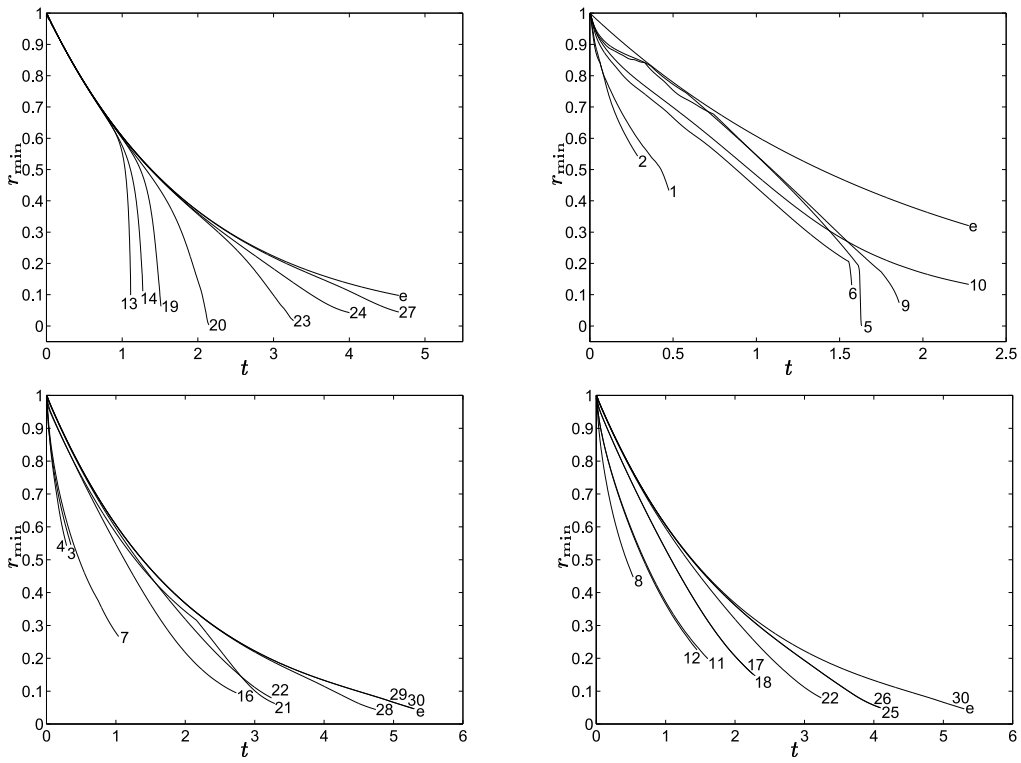

FIGURE 11. Minimum radii of the bridges versus time.

A first overview of the situation is given by figure 11, which presents the minimum radii of the stretched bridges for the various Weber and Capillary numbers as well as the "ideal" exponential curve (e) for comparison. The pictures clearly confirm the transitions between the different flow regimes.

The upper pictures in figure 11 show the transition from almost capillary dominated flow to more viscosity (upper left picture) or inertia (upper right picture) dominated flow regimes.

At low Capillary and Weber numbers (no. 13, 14, 19, 20, 23), the minimum bridge radii coincide with the ideal exp-function up to a limit of capillary stability. Beyond this limit, capillary instability leads to distortion of the bridge and the final breakup. The life time of a bridge is the longer the larger the Capillary number and the smaller the Weber number are. At the minimum of Capillary and Weber numbers (no. 13), the bridge breaks up just after $t = 1.0$. For higher Capillary numbers the breakup is delayed.

A totally different behavior can be seen for the transition from low Capillary and Weber numbers (no. 13, 14) to increased Weber numbers (no. 1, 2, 5, 6). While at small Weber numbers (no. 13, 14) the minimum bridge radii stay relatively close to the ideal exp-function during their whole life span, the radius functions at higher Weber numbers (no. 1, 2, 5, 6) deviate from the exp-function from the start. The life time of a bridge decreases and the deviation to the ideal case increases with increasing Weber number. The extreme examples (no. 1, 2) are strongly deformed and shortly living bridges.

REMARK 2. *Some of the bridges are strongly deformed from the start, yielding rather distorted meshes in the numerical simulations despite the mesh smoothing in* **Step 3** *of*

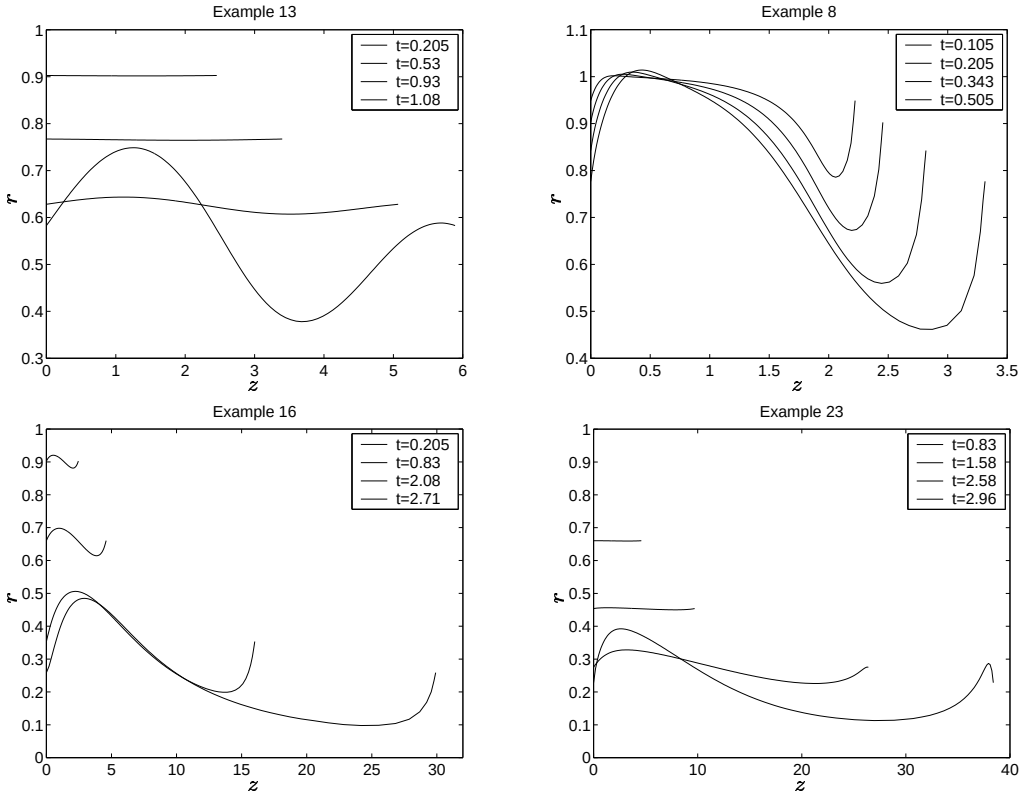

FIGURE 12. Bridge shapes for some representative examples: 13, 8 representing capillary and inertia dominated flow, respectively; 16, 23 representing the transitions from capillary to viscosity dominated and inertia to viscosity dominated flow, respectively.

the algorithm, see Section 2. This gives rise to a shorter "numerical" than physical life span of the corresponding bridges.

Figure 11 (lower pictures) shows the influence of decreasing Weber number and increasing Capillary number. It can be seen that for higher $Re = We/Ca$ (no. 3, 4, 7, 8, 11, 12, 16, 17, 18, 21) the minimum bridge radii are nowhere close to the ideal exp-function. The deviation from the ideal case increases at increasing Reynolds number. On the other hand, at lower Reynolds numbers, the minimum bridge radius is close to the ideal case and breakup is the more delayed the lower the Reynolds number.

Moreover, it is remarkable that the curves of minimum bridge radii are nearly identical for identical Reynolds numbers (no. 11/12, 17/18, 25/26, 29/30). This shows that capillary forces do not have a strong influence on the deformation behavior at higher Capillary or Weber numbers, $Ca > 0.75$ or $We > 0.17$, i.e. outside the capillary dominated regime.

In the rest of this section we discuss four representative examples, bridges no. 13, 8, 16 and 23, from the parameter field in more detail. The respective contour shapes of these bridges for several time instants are plotted in figure 12.

Bridge no. 13 at $Ca = 2.14 \cdot 10^{-3}$ and $We = 4.82 \cdot 10^{-4}$ represents capillary dominated flows. After the start, cp. $t = 0.205$, and during the main part of the stretching period, represented by e.g. the instant $t = 0.53$, a nearly ideal cylindrical shape exists. After this

the capillary instability induces a convex-concave shape leading to the final breakup of the bridge. The almost symmetric shape of the convex-concave distribution is an indication of the predominantly capillary driven instability, which by linear stability analysis is predicted to take on sinusoidal form.

Bridge no. 8 at $Ca = 7.50 \cdot 10^{-1}$ and $We = 1.69 \cdot 10^{1}$ represents inertia dominated flows. Already at the beginning of the stretching strong contour deformations develop close to the accelerated side. These disturbances are caused by the inertia of the fluid and are not significantly damped by viscous nor capillary forces during stretching. This contour deformation remains until the breakup of the bridge.

Bridge no. 16 at $Ca = 7.50 \cdot 10^{-1}$ and $We = 1.69 \cdot 10^{-1}$ represents the situation of balanced viscous and capillary forces and smaller inertia forces. The bridge develops only small deformations during stretching compared to, for instance, bridge no. 8. As can be seen from figure 12 at $t = 0.205$ a tiny convex-concave deformation is visible, which grows slowly during stretching. The deformation is caused by the dynamic pressure difference and is compensated by the capillary pressure. The stronger viscous forces in comparison to inertia forces prevent strong local deformations and flow variations, as seen for instance in example no. 8.

Bridge no. 23 at $Ca = 2.14 \cdot 10^{-1}$ and $We = 4.82 \cdot 10^{-4}$ shows an example for viscous dominated flows. The higher viscous forces in comparison to example no. 16 prevent strong local pressure variations inside the bridge and the bridge has a cylindrical shape during the main part of the stretching period. Just before the breakup a convex-concave deformation appears.

5.3. *Strain and Shear*

The evaluation of the strain and shear distribution inside the bridges provides a more refined view of the quality of the uniaxial extensional flows. In cylindrical coordinates, the strain rate $\dot{\epsilon}$ and the shear rate $\dot{\gamma}$ are given by

$$\dot{\epsilon} = \frac{2}{3}\Big(\partial_z v_z - \partial_r v_r\Big), \qquad \dot{\gamma} = \partial_r v_z + \partial_z v_r.$$

We are interested in the regions of Ω that are homogeneous with respect to the strain rate and shear rate. To this end we define the homogeneous part Ω_{hom} of Ω, where the deviation from the desired strain and shear rate distribution of the ideal bridge is less than 5 %:

$$\Omega_{hom}(t) := \{x \in \Omega(t) \mid \max\{|\dot{\epsilon}(t,x) - 1.0|, |\dot{\gamma}(t,x)|\} < 0.05\}, \tag{5.1}$$

as well as the fraction of the homogeneous part

$$\mathrm{hom}(t) := \frac{|\Omega_{hom}(t)|}{|\Omega(t)|}. \tag{5.2}$$

The latter expression is a direct measure for the quality of a stretched bridge. Figure 13 presents the values of *hom* as functions of time for the examples in the parameter field. For the sake of clarity some curves are omitted. The omitted curves are either close to those corresponding to neighbors in the parameter field or their values of *hom* are negligibly small for the whole stretching period (bridges no. 1, 2, 3, 4, 7, 8, 11, 12).

In order to get an even more condensed measure for the bridge qualities, we define the scalar quantity *qual*,

$$\mathrm{qual} := \int_0^{t_{breakup}} \mathrm{hom}(t)\, dt. \tag{5.3}$$

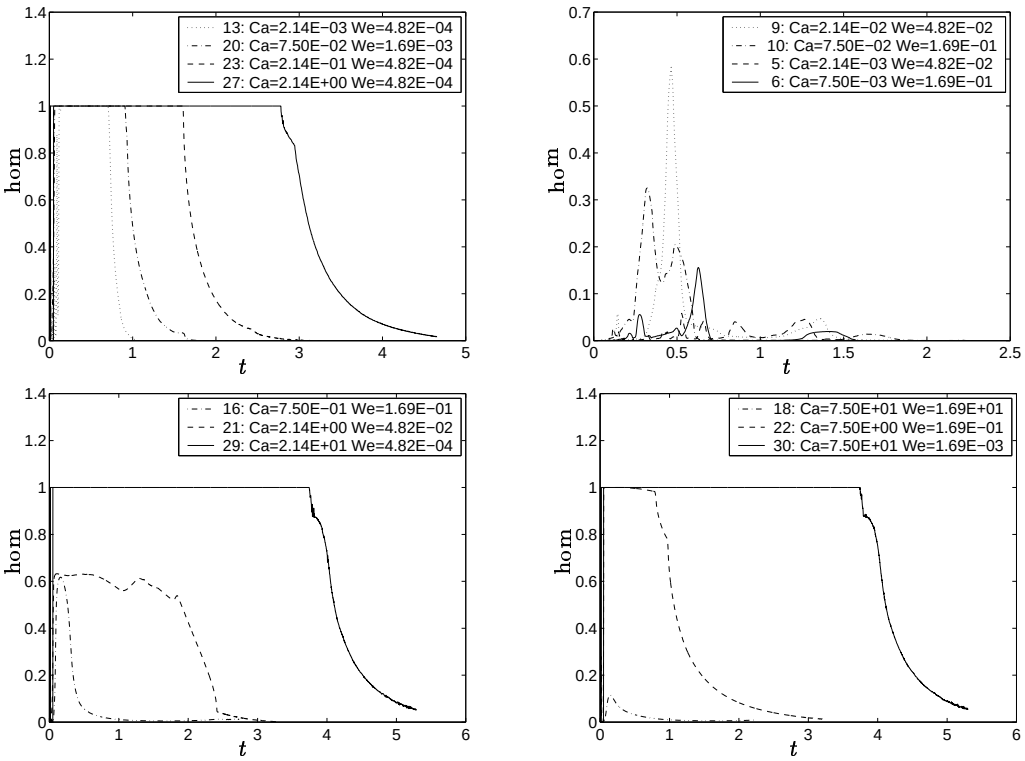

FIGURE 13. Homogeneous fraction $\mathrm{hom}(t) := \frac{|\Omega_{hom}(t)|}{|\Omega(t)|}$ of the domain for the examples in the parameter field.

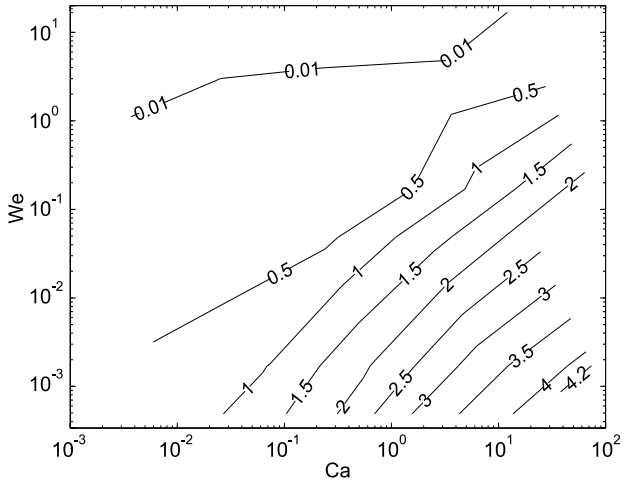

FIGURE 14. Contour plot of the quality measure qual, defined by (5.3).

From figures 11 and 13 a clear correspondence can be seen between the flow quality, characterized by *hom* and the bridge deformation, expressed by the function of minimum radius.

Comparing the curves in the upper left pictures of figures 11 and 13 (experiments no. 13, 20, 23, 27) shows that as long as the minimum radius follows the ideal exp-

function, i.e. there is no large deformation of the bridge, the flow inside the bridge enjoys a maximum homogeneity *hom*, which also means that the shear is minimum.

In the range of capillary dominated flows (e.g. bridges no. 13, 20) the homogeneous fraction vanishes just at the onset of the breakup of the bridge.

For higher Weber numbers (no. 5, 6, 9, 10), the bridge contours behave similar to example 16 in figure 12, exhibiting a convex-concave shape during stretching. These asymmetrical deformations result in rather small homogeneous fractions than for lower Weber numbers.

For viscosity dominated flows (no. 22, 29, 30), the homogeneous fraction is maximum and the shear rates remain minimum. This is caused by the strongly viscous transport of momentum, which inhibits strong deformations and variations of flow, hence the deformations are small and the bridge follows the ideal exponential case. On the other hand, for inertia dominated flows (no. 7, 8, 12, 18), the strong dynamic pressure gradients cause strong deformations and flow variations, resulting in large shear rates. The homogeneous fractions for these examples are extremely small. In the case of experiments no. 7, 8, 12, the homogeneous flow fraction remains close to zero and is therefore not drawn in figure 13.

To summarize, viscosity and inertia dominated flows exhibit very strong differences in the flow quality, expressed by the homogeneous fraction *hom*. Hence, the best regimes in terms of quality of the underlying extensional flow field is viscosity dominated flow at small Reynolds numbers.

But also in the case of small Capillary as well as small Reynolds numbers, where capillary forces dominate, the extensional flow is remarkably homogeneous up to the point of capillary driven breakup.

Let us also mention without explicitly showing corresponding curves that the shear rate is related to *hom*, i.e. the shear rate is high where *hom* is small and vice versa.

The scalar quantity *qual* confirms the increasing flow quality at decreasing Weber numbers and increasing Capillary numbers, cp. fig. 14. Large values of *qual* indicate the desirable situation of a large homogeneous flow fraction during a long time period.

Interestingly, *qual* remains almost constant at constant Reynolds numbers in the *We–Ca* parameter field. This behavior is most clearly visible for higher Capillary, where capillary forces are negligible. In this range, *qual* is a decreasing function of the Reynolds number only.

5.4. *Flow regimes and application*

In this section we discuss the strain and shear distributions for the four examples, bridges no. 13, 8, 16 and 23, in more detail and give further details for applications.

I Capillary dominated flow, bridge no. 13. As already seen above, even at small Capillary numbers and small Reynolds numbers homogeneous flow can be realized during almost the whole period of stretching. For instance bridge no. 13, includes a homogeneous strain flow immediately after the start. Figures 15 and 16 show the strain and shear rate distribution inside this bridge at different time instants.

Just after the start, cp. $t = 0.08$ in figure 15, viscous momentum transport from the membranes into the bridge causes a weak strain variation and a weak shear flow fraction, which are damped down quickly by the capillary forces that are strong compared to inertia and viscous forces.

During the main part of the stretching period, represented by e.g. the instant $t = 0.58$, an ideal extensional flow exists, until capillary forces initiate strong variations in strain and shear rates, cp. $t = 0.98$, which lead to the final capillary dominated breakup.

As long as the bridge maintains an ideal cylindrical shape, the extensional flow is perfectly homogeneous inside the bridge. After this the capillary instability induces a deformed shape, see figure 12. In the concave part of the bridge the strain rate increases, while in the convex part the strain rate decreases, see figures 15, 16.

Eventually, at the end of the stretching period, strong variations in strain rate and high values of the shear rate lead to a quickly vanishing *hom*, see figure 13.

We conclude that homogeneous strain experiments in the range of small Reynolds numbers and small Capillary numbers are possible up to capillary breakup.

II Inertia dominated flow at high Weber and Capillary numbers, bridge no. 8. Bridge no. 8 represents a less suited regime for homogeneous extensional flow. Figures 17 and 18 show the strain and shear rate distribution inside the bridge at different time instants.

Already at $t = 0.05$ strong flow variations have developed close to the accelerated side. Since viscous (diffusive) momentum transport inside the bridge is weak, the forces lead to a strong contour necking.

In the left, convex part of the bridge the strain rate is much below the desired strain rate of unity. This example shows that inertia dominated flow at high Weber and Capillary numbers is prohibitive for homogeneous strain flow.

III Balanced viscous and capillary forces at smaller inertia forces, bridge no. 16. Studying bridge no. 16, we see that this range of parameters provide more suitable conditions for homogeneous extensional flow.

Figures 19 and 20 show the strain and shear rate distribution inside the bridge at different time instants. The bridge develops only small flow variations during stretching.

Despite of the better flow quality in comparison to example no. 8, figure 13 confirms that almost no homogeneous flow exists inside the bridge for the main part of the stretching period. However, since the flow variations are weak in the convex part, a local shear free strain flow exists for some time, which may be used for strain experiments.

IV Low Weber numbers, medium Capillary numbers, bridge no. 23. As pointed out above, the most suitable parameters for homogeneous extensional flow are in the range of viscous flows at small capillary forces. Such parameters at high Capillary numbers and small Reynolds numbers are only realizable at very high fluid viscosity, which may not be available in experiment.

Therefore, a more practicable example (bridge no. 23) at medium viscosity, or in non-dimensional terms, medium Capillary number is presented in figures 21 and 22.

The figures show the strain and shear rate distribution inside this bridge at different time instants. The higher viscous forces in comparison to the previous example prevent strong local pressure variations inside the bridge. Therefore, the bridge remains cylindrical and the flow homogeneous during the main part of the stretching period. Just before the breakup variations in the strain and shear rates appear.

The very weak flow variations demonstrate the excellent flow quality, which makes a bridge at low Reynolds number and even medium Capillary number suitable for strain experiments.

Examples I – IV reveal that small inertia forces in comparison to viscous and capillary forces are necessary for the realization of homogeneous uniaxial extensional flow.

As outlined above, the parameter regime providing most suitable conditions for continuous homogeneous extensional flow at negligible gravity forces is found at low Reynolds

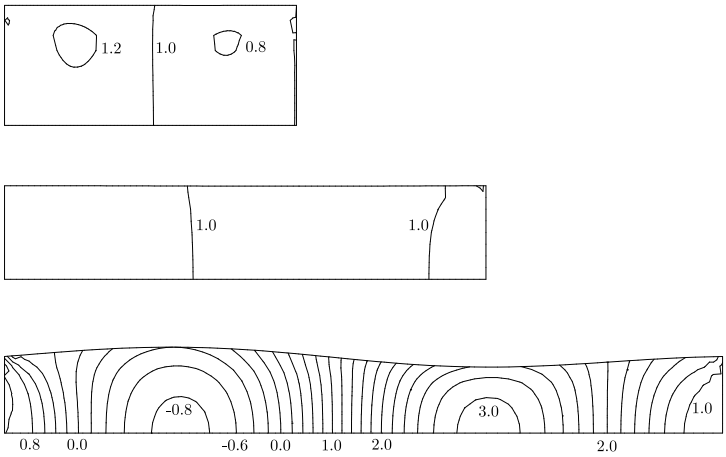

FIGURE 15. Bridge no. 13: Strain rate distribution at $t = 0.08$, $t = 0.58$ and $t = 0.98$, from top to bottom respectively; distance of levels for the plotted isolines: 0.2.

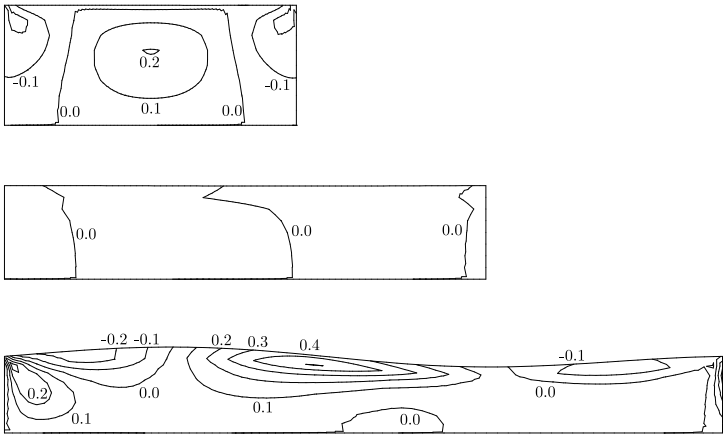

FIGURE 16. Bridge no. 13: Shear rate distribution at $t = 0.08$, $t = 0.58$ and $t = 0.98$, from top to bottom respectively; distance of levels for the plotted isolines: 0.1.

numbers and high Capillary numbers. Unfortunately, these parameters cause certain difficulties in practice. High Capillary numbers and small Reynolds numbers are only realizable at very small bridge dimensions and very high fluid viscosity. High viscosity causes severe difficulties in handling the fluid or those fluids may not even be available. Therefore, extensional flow experiments are mainly performed at medium or low Capillary numbers, where the duration of homogeneous flow is limited in space and time.

Moreover, in the range of small Reynolds as well as small Capillary numbers, where inertia forces are smaller than viscous and capillary forces, the experimental realization of homogeneous extensional flows is indeed restricted by further difficulties.

For instance the duration of the ideal homogeneous flow varies with the characteristic numbers, cp. figure 13. The examples reveal that at decreasing Capillary numbers stronger capillary forces (compared to viscous forces) lead to a shorter life time of the homogeneous flow. This is also confirmed by the plot of minimum radii in figure 11, where the breakup time decreases at decreasing Capillary numbers.

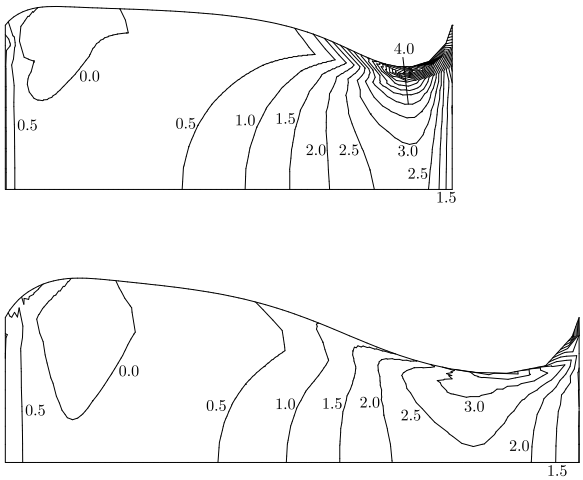

FIGURE 17. Bridge no. 8: Strain rate distribution at $t = 0.05$ and $t = 0.455$, from top to bottom respectively; distance of levels for the plotted isolines: 0.5.

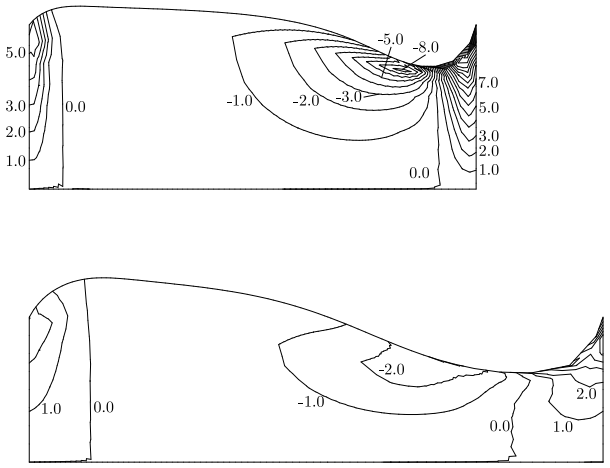

FIGURE 18. Bridge no. 8: Shear rate distribution at $t = 0.05$ and $t = 0.455$, from top to bottom respectively; distance of levels for the plotted isolines: 1.0.

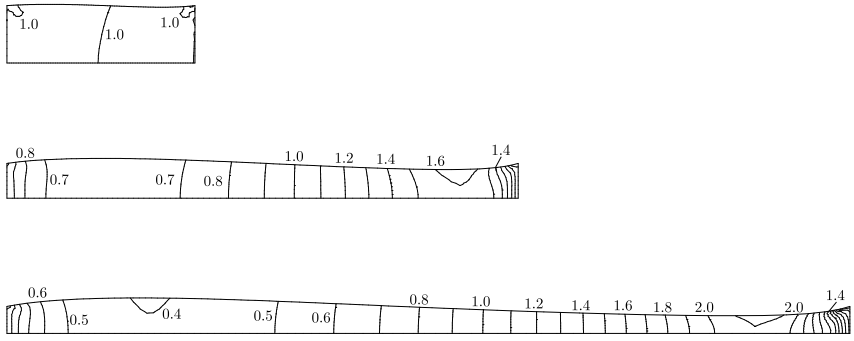

FIGURE 19. Bridge no. 16: Strain rate distribution at $t = 0.205$, $t = 1.205$ and $t = 1.705$, from top to bottom respectively; distance of levels for the plotted isolines: 0.1.

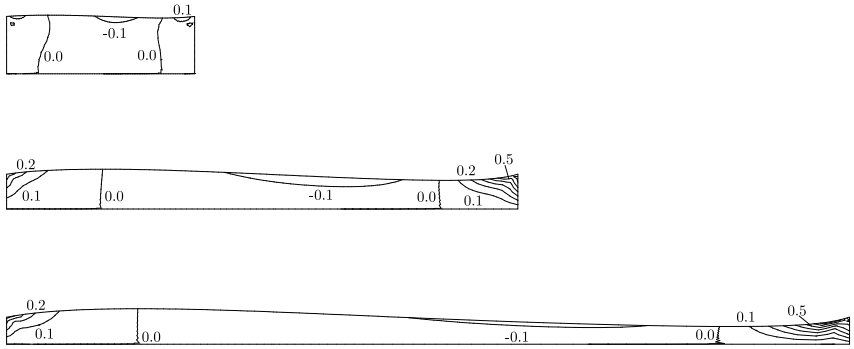

FIGURE 20. Bridge no. 16: Shear rate distribution at $t = 0.205$, $t = 1.205$ and $t = 1.705$, from top to bottom respectively; distance of levels for the plotted isolines: 0.1.

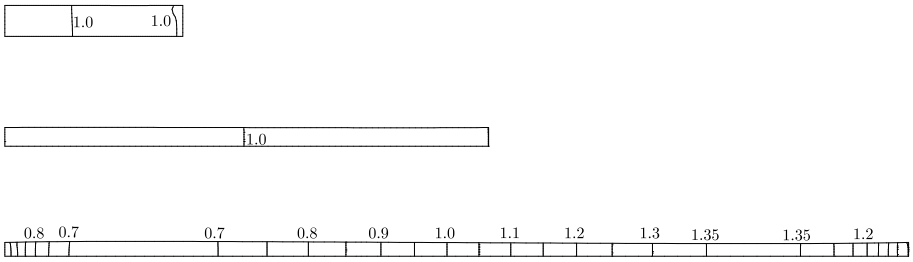

FIGURE 21. Bridge no. 23: Strain rate distribution at $t = 0.58$, $t = 1.58$ and $t = 2.205$, from top to bottom respectively; distance of levels for the plotted isolines: 0.05.

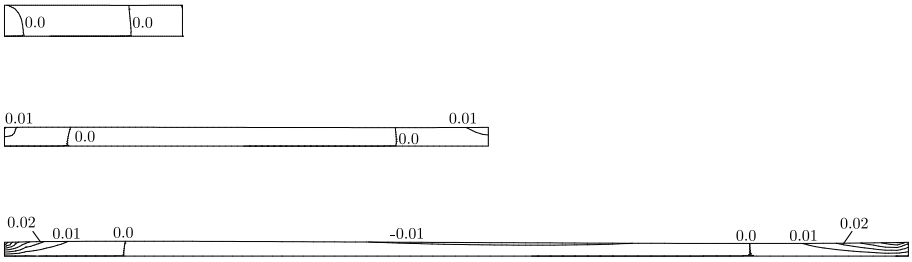

FIGURE 22. Bridge no. 23: Shear rate distribution at $t = 0.58$, $t = 1.58$ and $t = 2.205$, from top to bottom respectively; distance of levels for the plotted isolines: 0.01.

6. Conclusion

We have investigated the possibility to generate nearly homogeneous uniaxial extensional flows with an almost constant strain rate in a stretched liquid bridge under μ-g conditions. The key ingredient of the method is the adaptation of the disk diameters in order to have always ideal boundary conditions to hold a cylindrical fluid bridge. This method causes much weaker end-effects at the bridge than the commonly used method with unchangeable disks.

But even under these optimal conditions, the liquid bridges are deformed by forces owing to fluid inertia and surface tension. The balances between inertia and surface tension forces, expressed by the Weber number, and between viscous and surface tension forces, expressed by the Capillary number, determine the deformation and flow behavior.

Our investigations present systematically different deformations and flow qualities in dependence on Ca, We and $Re = We/Ca$. Regions of *capillary dominated flow*, $Ca \ll 1$,

$We \ll 1$, *viscosity dominated flow*, $Ca > \mathcal{O}(0.1)$, $Re < \mathcal{O}(0.1)$, and *inertia dominated flow*, $We > \mathcal{O}(0.1)$, $Re > \mathcal{O}(0.1)$ were detected, which exhibit totally different bridge deformations during stretching.

In the range of *capillary dominated flow*, ideal extensional flows exist during the main part of the stretching period, until capillary forces initiate strong variations in strain and shear rates to the final capillary dominated breakup. As long as the bridge maintains an (almost) ideal cylindrical shape, the extensional flow is (nearly) perfectly homogeneous inside the bridge. In the range of small Capillary numbers and small Reynolds numbers, homogeneous strain experiments are possible up to capillary breakup. However, weak viscous forces (compared to capillary ones) do not essentially delay the capillary dominated breakup. Therefore the period of ideal flow is limited in this case.

In the range of *inertia dominated flow*, strong flow variations and contour deformations occur, which are caused by the fluid inertia and are not damped by viscous nor capillary forces during stretching. This is the most unsuitable regime for homogeneous extensional flow.

Most suitable parameters for homogeneous extensional flow are in the range of *viscosity dominated flow*. The high viscous forces in comparison to inertia and capillary forces prevent strong local pressure variations inside the bridge. Therefore, the bridge remains cylindrical and the flow homogeneous and constant during a long stretching period.

In experiment, such parameters of high Capillary numbers and small Reynolds numbers may not always be realizable, because of the fluid properties or bridge geometry. In this case, our discussion of the flow quality allows for an estimation of the expected flow quality, expressed by the quantity *qual* in dependence on the parameters Ca and We, see for instance figure 14.

REFERENCES

Bänsch, E. 1991 An Adaptive Finite-Element-Strategy for the Three-Dimensional Time-Dependent Navier-Stokes Equations. *J. Comp. Appl. Math.* **36**, 3–28.

Bänsch, E. 1998 Simulation of instationary, incompressible flows. *Acta Math. Univ. Comenianae* **LXVII**, no. 1, 101–114.

Bänsch, E. 2001 Finite element discretization of the Navier–Stokes equations with a free capillary surface. *Numer. Math.* **88**, 203-235.

Berg, S., Kröger, R. & Rath, H. J. 1994 Measurement of extensional viscosity by stretching large liquid bridges in microgravity. *J. Non–Newtonian Fluid Mech.* **55**, 307–319.

Berg, C. P., Dreyer, M. & Rath, H. J. 1999 A large fluid–bridge device to measure the deformation of drops in uniaxial extensional flow fields. *Meas. Sci. Technol.* **10**, 956–964.

Berg, C. P. 2002 Tropfendeformation in monoaxialer und ebener Dehnströmung, (in German). PhD Thesis, University of Bremen, Shaker Verlag.

Bristeau, M. O., Glowinski, R. & Periaux J. 1986 Numerical methods for the Navier–Stokes equations. Application to the simulation of compressible and incompressible flows. *Computer Physics Report* **6** 73–188.

Chin, H. B. & Han, C. D. 1979 Studies on droplet deformation and breakup. I. Droplet deformation in extensional flow. *J. Rheol.* **23**, no. 5, 557–590.

Gaudet, S., McKinley, G. H. & Stone, H. A. 1996 Extensional deformation of Newtonian liquid bridges. *Phys. Fluids* **8**, no. 10, 2568–2579.

Higdon, J. J. L. 1993 The kinematics of the four–roll mill. *Phys. Fluids A* **5**, no. 1, 274–276.

Kröger, R., Berg, S., Delgado, A. & Rath, H. J. 1992 Stretching behaviour of large polymeric and Newtonian liquid bridges in plateau simulations. *J. Non–Newtonian Fluid Mech.* **45**, 385–400.

Lailly, P. 1976 Résolution Numérique des Équations de Stokes en Symétrie de Révolution par une Méthode d'Éléments finis non Conformes. PhD thesis, Paris.

Maia, J. M., Covas, J. A., Nóbrega, J. M., Dias, T. F. & Alves, F. E. 1999 Measure

uniaxial extensional viscosity using a modified rotational rheometer. *J. Non–Newtonian Fluid Mech.* **99**, 183–197.

MATTA, J. E. & TYTUS, R.P. 1988 Liquid stretchin using a falling cylinder. *J. Non–Newtonian Fluid Mech.* **30**, 1–19.

MEISSNER, J. 1969 Rheometer zur Untersuchung der deformationsmechanischen Eigenschaften von Kunststoff-Schmelzen unter definierter Zugbeanspruchung (in German). *Rheol. Acta* **8**, 78–88.

MIGHRI, F., AJJI, A. & CARREAU, P. J. 1997 Influence of elastic properties on drop deformation in elongational flow. *J. Rheol.* **41**, 1183–1201.

PLATEAU, J. 1863 Experimental and theoretical researches on the figures of equilibrium of a liquid mass withdrawn from the action of gravity, etc. Annual Report of the Board of Regents of the Smithsonian Institution, Pt. 1, House of Representatives Misc. Doc. **83**, 38th Congress, 1st Session, 207–285.

RAYLEIGH, LORD 1878 On the instability of jets. *Proc. Lond. Math. Soc.* **4**, 10.

SPIEGELBERG, S. H., ABLES, D. C. & MCKINLEY, G. H. 1996 The role of end–effects on measurements of extensional viscosity in filament stretching rheometers. *J. Non-Newtonian Fluid Mech* **64**, 229–267.

SRIDHAR, T., TIRTAATMADJA, V., NGUYEN, D. A. & GUPTA, R. K. 1991 Measurement of extensional viscosity of polymer solutions. *J. Non–Newtonian Fluid Mech.* **40**, 271–280.

STONE, H. A. 1994 Dynamics of drop deformation and breakup in viscous fluids. *Annual Rev. Fluid Mech.* **26**, 65–102.

TIRTAATMADJA, V. & SRIDHAR, T. 1993 A Filament Stretching Device for Measurement of Extensional Viscosity. *J. Rheol.* **37**, 1081–1102.

TENHAEFF, M. 1997 Computation of incompressible, axially symmetric flows in electrically conducting fluids under influence of rotating magnetic fields, (in German). Master thesis, Albert–Ludwigs–Universität, Freiburg i. Br.

YAO, M. & MCKINLEY, G. H. 1998 Numerical simulation of extensional deformations of viscoelastic liquid bridges in filament stretching devices. *J. Non–Newtonian Fluid Mech.* **74**, 47–88.

YAO, M., SPIEGELBERG, S. H. & MCKINLEY, G. H. 2000 Dynamics of weakly strain-hardening fluids in filament stretching devices. *J. Non–Newtonian Fluid Mech.* **89**, 1–43.

ZHANG, X., PADGETT, R. S. & BASARAN O. A. 1996 Nonlinear deformation and breakup of stretching liquid bridges. *J. Fluid Mech.* **329**, 207–245.